ACS Photonics

pubs.acs.org/journal/apchd5

Article

Vertical Architecture Solution-Processed Quantum Dot Photodetectors with Amorphous Selenium Hole Transport Layer

Atreyo Mukherjee,[†] Haripriya Kannan,[†] Le Thanh Triet Ho, Zhihang Han, Jann Stavro, Adrian Howansky, Neha Nooman, Kim Kisslinger, Sébastien Léveillé, Orhan Kizilkaya, Xiangyu Liu, Håvard Mølnås, Shlok Joseph Paul, Dong Hyun Sung, Elisa Riedo, Abdul Rumaiz, Dragica Vasileska, Wei Zhao, Ayaskanta Sahu,* and Amir H. Goldan*

Cite This: *ACS Photonics* 2023, 10, 134−146

Read Online

ACCESS | Metrics & More | Article Recommendations | Supporting Information

ABSTRACT: Colloidal quantum dots (CQDs) provide wide spectral tunability and high absorption coefficients owing to quantum confinement and large oscillator strengths, which along with solution processability, allow a facile, low-cost, and room-temperature deposition technique for the fabrication of photonic devices. However, many solution-processed CQD photodetector devices demonstrate low specific-detectivity and slow temporal response. To achieve improved photodetector characteristics, limiting carrier recombination and enhancing photogenerated carrier separation are crucial. In this study, we develop and present an alternate vertical-stack photodetector wherein we use a solution-processed quantum dot photoconversion layer coupled to an amorphous selenium (*a*-Se) wide-bandgap charge transport layer that is capable of exhibiting single-carrier hole impact ionization and is compatible with active-matrix readout circuitry. This *a*-Se chalcogenide transport layer enables the fabrication of high-performance and reliable solution-processed quantum dot photodetectors, with enhanced charge extraction capabilities, high specific detectivity (D^* ~ 0.5−5 × 10^{12} Jones), fast 3 dB electrical bandwidth (3 dB BW ~ 22 MHz), low dark current density (J_D ~ 5−10 pA/cm^2), low noise current (i_n ~ 20−25 fW/$Hz^{1/2}$), and high linear dynamic range (LDR ~ 130−150 dB) across the measured visible electromagnetic spectrum (~405−656 nm).

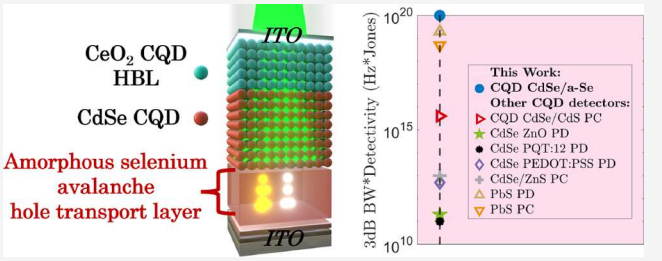

KEYWORDS: *cadmium selenide quantum dots, colloidal quantum dot photodetectors, vertical-stack photodetectors, amorphous hole transport layer, avalanche transport layer, avalanche photodiodes*

INTRODUCTION

Recent progress in comprehending the science behind solution-processed materials and their interfaces has led to an improved performance in a number of applications, namely, light-emitting diodes,[1] lasers,[2] solar cells,[3] infrared photodetectors,[4] and X-ray applications.[5] In recent years, CQDs with optoelectronic tunability and facile solution processability are on the rise to harness a desired spectral range.[6] This low-cost and room-temperature fabrication technique facilitates ready integration with an almost limitless variety of substrates (conducting or insulating, crystalline or amorphous, rigid or flexible), including postprocessing atop integrated electronic-readout circuitry.[7,8] In comparison, single-crystalline elemental (silicon) and compound semiconductors (InGaAs/GaAs) require high-temperature processing and high vacuum conditions, while monolithically integrated optoelectronics mandate growth on crystalline substrates using lattice-matched semiconductors, once again accompanied by high cost equipment.[9] With the ease of room-temperature deposition, CQD photodetectors can be fabricated in one of three architectures: phototransistors, photoconductors or photodiodes.[10] Among these, phototransistors (PT; amplifying switches through a gate-programmable semiconducting channel) are lateral devices (large thermal budget and footprint) that complicate the integration of pixel-based digital imaging and are essentially used as optical sensors. Although photoconductors (PC) allow circulation of only one type of carrier through multiple cycles to reach high gains before recombination, they suffer from a slow temporal response (1−3000 Hz).[9−11] In comparison, photodiodes (PD) are based on *p-n* or *p-i-n* junctions that have a built-in potential facilitating the extraction of photogenerated carriers, have a faster temporal response, can demonstrate high gains through impact

Received: August 30, 2022
Published: December 29, 2022

https://doi.org/10.1021/acsphotonics.2c01353
ACS Photonics 2023, 10, 134−146

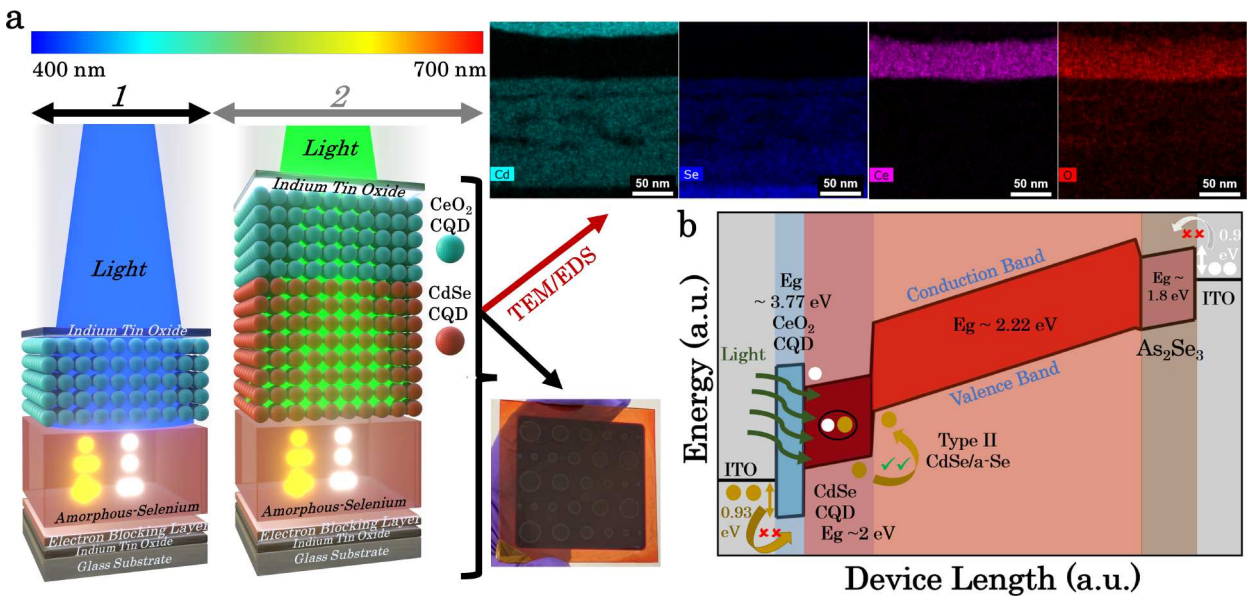

Figure 1. (a) [left] Schematic showing the *a*-Se avalanche transport layer. It can either be used as an avalanche photon absorbing/photoactive layer (device 1) or a HTL with avalanche capabilities (device 2). This unique chalcogenide material can be used to make efficient vertical geometry hybrid solution-processed/*a*-Se detectors with applications covering the entire visible electromagnetic spectrum. The visible-light sensitive CdSe CQD layer (device 2) is coupled to the wide-band gap *a*-Se layer that prevents electrical shorts due to voids/cracks in the CdSe CQD film. The added CeO_2 CQD HBL in devices 1 and 2 increases the Schottky injection barrier and decreases the J_D. TEM cross-sectional images are shown. EDS cross-sectional images were used to characterize the elemental composition of the detector (top right). Also shown is a picture of our fabricated detector device 2. (b) Simulated energy band diagram of the device under an applied bias.

ionization avalanche, and their inherent vertical photodetector geometry has a lower footprint as compared to lateral structures that can be easily integrated onto a read-out chip for digital imaging applications.[9] Here, we propose utilizing an *a*-Se hole transport layer (HTL) to enhance the performance of vertical geometry CQD PDs by enhanced hole carrier extraction and with a potential toward large-scale fabrication on read-out circuits.

a-Se is a wide-band gap semiconductor ~ 2.22 eV, which can demonstrate single carrier hole avalanche gain (vacuum tube systems gain ~ 1000 and solid-state system gain ~ 50−100),[12,13] with a reported ultralow J_D at the onset of impact ionization ~ 30 pA/cm^2[12,14] and measured non-Markov excess noise factors below 2 (see Supporting Information (SI), section S1).[15−18] Moreover, this chalcogenide disordered material offers the ease of large-scale fabrication and, thus, has been commercialized as a direct-conversion vertical geometry X-ray detector material providing high spatial resolution for applications in 2D and 3D mammography.[12] Recently, *a*-Se is also emerging as a viable low-cost solid-state imager with an avalanche gain to be utilized in indirect conversion positron emission tomography and high-energy physics applications.[19]

Figure 1a shows schematic representations of two *a*-Se-based vertical geometry photodetector systems numbered 1 and 2. Both of these structures utilizes ITO as the transparent top electrode. Device schematic 1 is responsive in the spectrum window between 400 and 450 nm and utilizes *a*-Se as a photoactive hole avalanche layer coupled to a solution-processed CeO_2 CQD hole blocking layer (HBL). It was our first demonstration of the coupling of *a*-Se and solution-processed CQDs. CeO_2 CQD HBL was used as an efficient noninsulating and nearly stoichiometric *n*-type HBL (permittivity ~ 30 and an enhanced bandgap ~ 3.77 eV: limits Schottky injection from the electrodes, prevents Joule heating, and hinders the irreversible breakdown of the device) in the desired *p-i-n* vertical geometry system, demonstrating an avalanche gain of ~42 and the lowest measured J_D of ~30 pA/cm^2 at the onset of avalanche.[12,16,20] With our first successful coupling of CQDs and *a*-Se achieving gain, in this work we proceed to utilize *a*-Se as a HTL with a spectrally tunable solution-processed CdSe CQD as a photon absorption layer (Figure 1a, device 2). To enable fast and sensitive photodetection, photocarrier recombination needs to be limited during the transport process by physically separating the photogenerated hole and electron carriers,[11] and here we show the design of hybrid photodetectors where optical absorption and charge transport are physically separated, thus enabling increased flexibility for spectral tuning and increased charge extraction.[21] Elemental analysis was performed on the sample using cross-sectional transmission electron microscopy energy-dispersive X-ray spectroscopy (TEM-EDS) images, as shown in Figure 1a. The layer thicknesses have been summarized in SI, section S2 and Table S1. The remaining device stack is similar for devices 1 and 2 in Figure 1a. Our detectors use an inorganic electron blocking layer (EBL). Due to a high density of traps (deep trap density ~ 10^{19} cm^{-3}, see Table S1), the electron mobility in the EBL is extremely small, 10^{-5} cm^2/V·s. This limits the injected electrons from reaching the *a*-Se layer.[20] The detectors were fabricated on 75 nm ITO coated substrates. Figure 1b shows the technology for computer-aided design (TCAD) simulated energy-band diagram of the device under applied bias (see SI, section S2 and Figure S2, for further details on the Silvaco ATLAS simulation framework). Light is incident and absorbed directly by the photoactive CdSe CQD layer through the transparent *n*-type CeO_2 HBL layer with a measured bandgap of ~3.77 eV.[12] The type-II heterostructure formed between *a*-Se and CdSe CQDs enables maximum extraction of photogenerated holes. Our hybrid *a*-Se-based CQD photodetector demonstrates the

https://doi.org/10.1021/acsphotonics.2c01353
ACS Photonics 2023, 10, 134−146

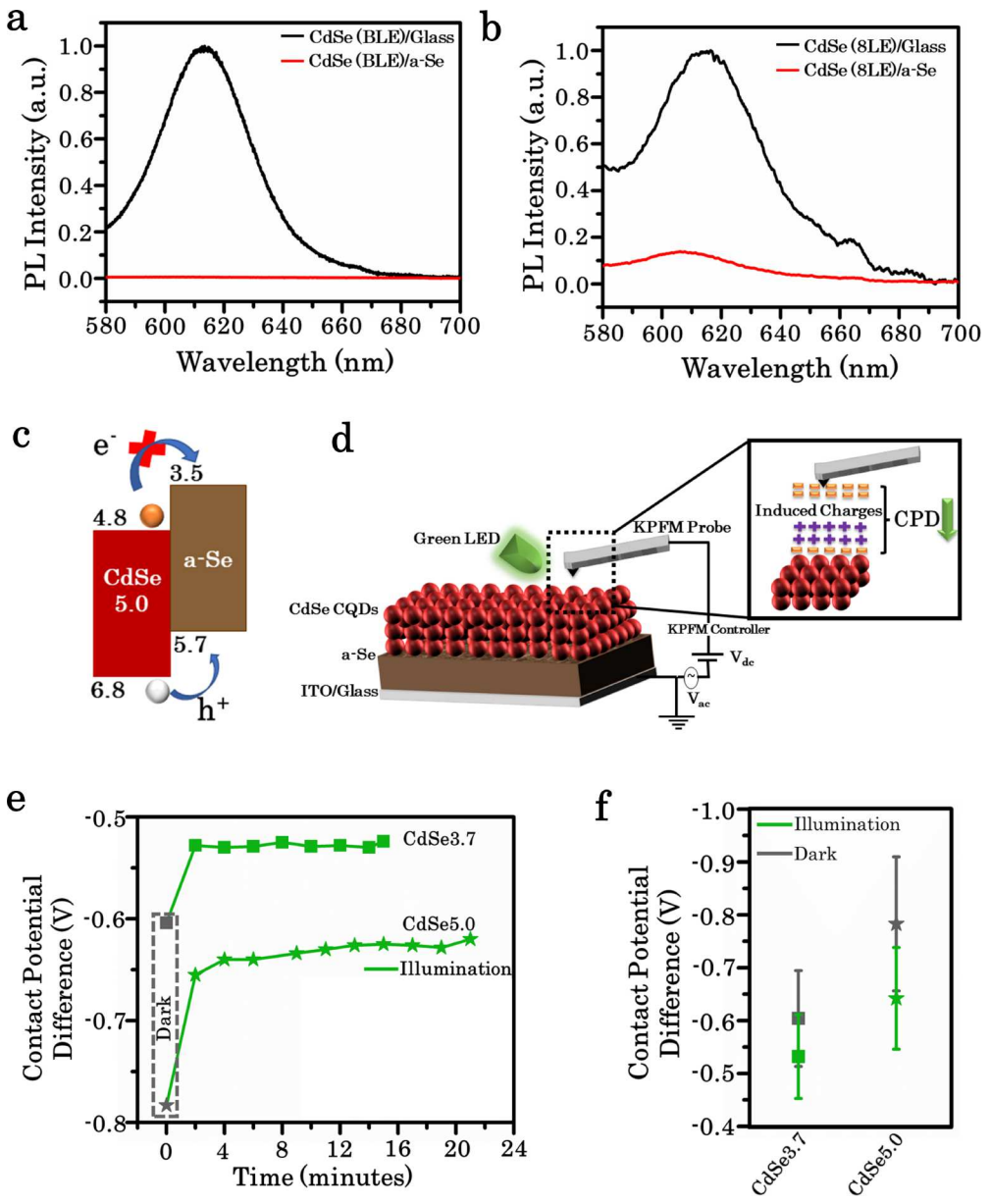

Figure 2. Charge-transfer characterization in photoluminescence spectroscopy: (a) Effective emission quenching of as-synthesized CdSe3.7 on *a*-Se against CdSe3.7 CQDs on glass (b) after ligand exchanged (8LE) layer-by-layer, as in the fabricated device. (c) Band-alignment of CdSe5.0 with respect to *a*-Se showing favorable band alignment for hole-transfer. (d) Schematic of the CdSe/*a*-Se/ITO heterostructure for KPFM measurements to identify the type of charge-transfer. Inset shows induced positive charges on CdSe after thermal equilibrium in dark and negative charges left by hole-transfer compensates for the induced positive charge after excitation, thus reducing CPD. (e) The results show the CPD reaches saturation after 10 min of green-light illumination for CdSe3.7/*a*-Se, and CdSe5.0/*a*-Se devices at dark and at illumination. (f) The decrease in the absolute value of CPD upon green light illumination suggests the transfer of holes over electrons in the CdSe/*a*-Se heterostructure. At dark: CdSe3.7/*a*-Se = −0.604 ± 0.09 V; CdSe5.0/*a*-Se = −0.783 ± 0.13 V. After illumination: CdSe3.7/*a*-Se = −0.532 ± 0.08 V; CdSe5.0/*a*-Se = −0.642 ± 0.09 V.

best-in-class performance, that is, a detectivity-bandwidth product of ∼10^{20} Jones × Hz in the visible light electromagnetic spectrum range.

RESULTS AND DISCUSSION

Solution-processed colloidal CdSe QDs were synthesized using a modified procedure by Kang et al.[22] To study the effect of CQD size on device performance, nanocrystals of multiple sizes were synthesized and studied. Further details on the material characterization of studied QDs is provided in SI, section S3 (Figure S3). Here, we present results on two sets of particle sizes with average particle diameters of 3.7 and 5.0 nm, respectively. Here on, these two dot sizes will be addressed as CdSe3.7 and CdSe5.0, respectively.

For the CdSe/*a*-Se heterostructure, we investigated the charge-transfer characteristics using photoluminescence (PL) quenching, ultraviolet photoelectron spectroscopy (UPS), and kelvin-probe force microscopy (KPFM)[23−25] to validate our hypothesis that *a*-Se is an excellent HTL for CQD-based photodetectors. PL spectroscopy was carried out to study if emission quenching takes place to effectively conclude the charge transfer between the active layer (CdSe CQD) and HTL (*a*-Se). All the emission measurements were normalized to the absorbance to account for the possible particle density

https://doi.org/10.1021/acsphotonics.2c01353
ACS Photonics 2023, 10, 134−146

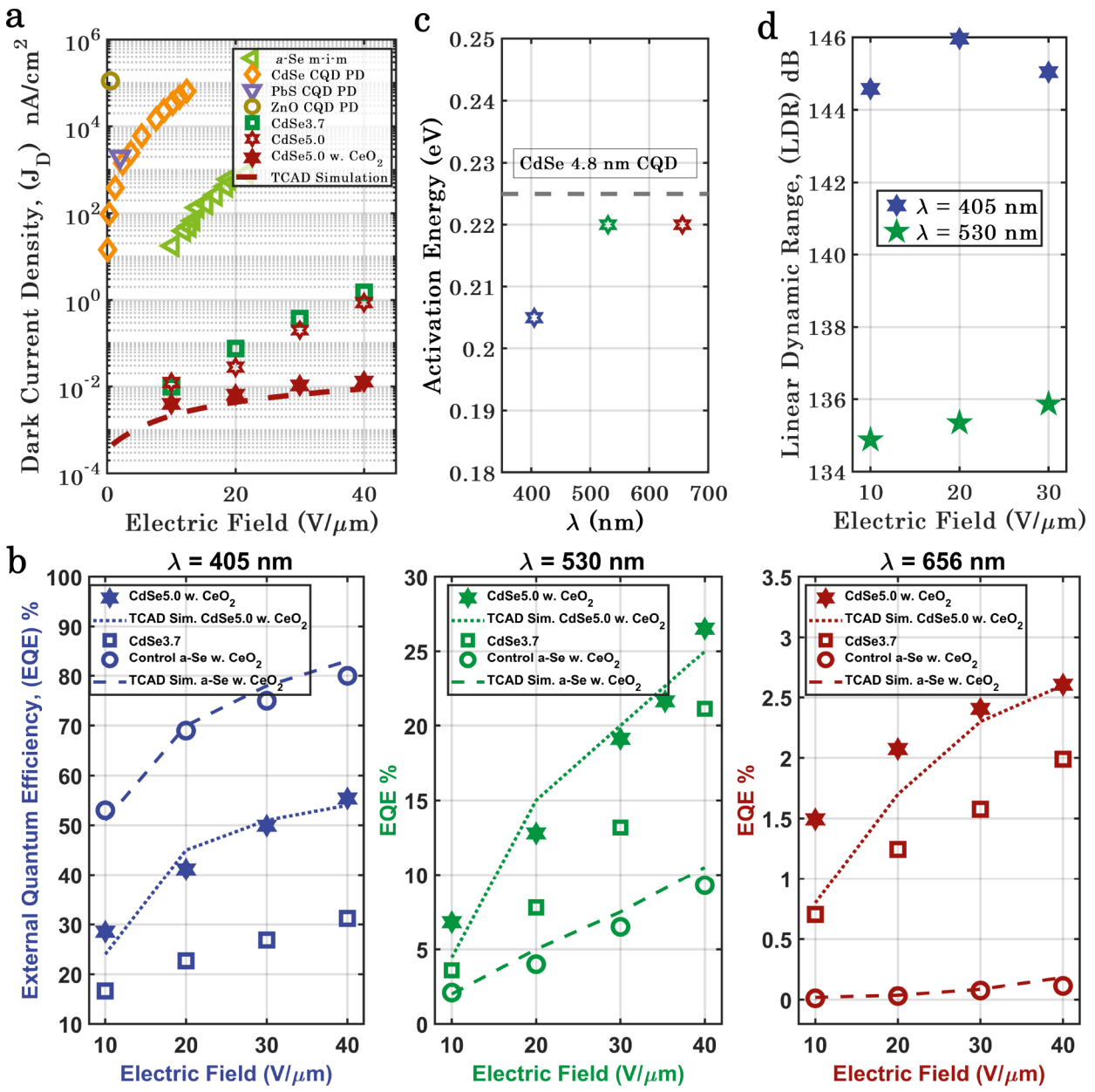

Figure 3. (a) Measured J_D in the *p-i-n* CdSe3.7/*a*-Se and CdSe5.0/*a*-Se detector structure. Best results were obtained when an added CeO_2 CQD HBL was used for the CdSe5.0/*a*-Se CQD-based detector structure. J_D results were also compared with *a*-Se detectors sandwiched between metal electrodes,[32] CdSe CQD-based photodetectors,[33] PbS CQD photodiodes,[34] and ZnO photodiodes.[35] (b) Measured external quantum efficiency, EQE (%) for blue (405 nm), green (530 nm), and red (656 nm) light, in the *p-i-n* CdSe3.7/*a*-Se and CdSe5.0/*a*-Se with CeO_2 HBL detector structure, and a control sample without the CdSe CQD layer with *a*-Se as the photon absorption layer.[34] Silvaco, ATLAS TCAD simulations were used to validate the experimentally measured EQE. (c) Simulation validation of activation energy for singlet exciton dissociation to free e/h pairs in CdSe5.0 compared with previous wavelength independent reports in 4.8 nm CdSe QDs by Elward Et al.[36] (d) Measured linear dynamic range (dB) in the best performing CdSe5.0/*a*-Se with CeO_2 HBL detector structure. All device measurements were performed at room temperature (295 K).

difference on glass and on *a*-Se (SIsection S4, Figures S4 and S5).[26]Figure 2a shows emission quenching of 99% in the as-synthesized CdSe3.7/*a*-Se heterostructure referred to as "before ligand-exchange (BLE)", and Figure 2b shows nearly ~87% quenching efficiency for the layer-by-layer (8×) ligand-exchanged (8LE) CdSe3.7/*a*-Se heterostructure. Similarly, the CdSe5.0 thin-film spin-coated on *a*-Se films showed nearly 96% PL quenching for as-synthesized CdSe CQDs, as shown in SI, section S4, Figure S6(a). Scaling up the thickness of CdSe5.0 by ligand-exchanging CQDs layer-by-layer (7×, (7LE)) on *a*-Se also shows an efficient emission quenching of 91%, which is representative of the charge transfer at the interface of CdSe/*a*-Se (SIsection S4, Figure S6(b)). In order to prove the type of charge transfer (holes or electrons), the band offset between CdSe and *a*-Se was studied using KPFM and UPS techniques.

As a starting point, a comparison of band-edges between bulk CdSe and *a*-Se was carried out to observe if the device architecture would form a type-I or type-II heterostructure. For bulk CdSe, the work function is expected to be around 5.35 eV with a valence band maximum between 6−6.8 eV (see SI, section S5).[27] In CQDs, however, the band-edges can be significantly modified owing to quantum confinement as well as due to ligand surface chemistry. A simple calculation on

https://doi.org/10.1021/acsphotonics.2c01353
ACS Photonics 2023, 10, 134−146

expected band-edges based on Brus equation (as detailed in SIsection S5)[28,29] demonstrated that CdSe CQDs and *a*-Se form a type-II heterostructure with energetically favorable band-offset for holes. To figure out the valence band edge of CdSe CQDs experimentally, we used a combination of KPFM and UPS. Work-function of CdSe CQDs was measured using KPFM, followed by measurement of valence band maximum in UPS and conduction band minimum with optical absorption spectroscopy. KPFM works on the principle of the parallel-plate capacitor and maps the surface potential (also known as contact potential difference (CPD)) which equals the work-function difference of the sample and probe. Unlike UPS, KPFM can be used to determine the work function of insulators as well. SIsection S6, Figure S7(a),(b) shows KPFM surface potential maps for CdSe3.7 and CdSe5.0. These surface potential maps were then used to obtain the average contact-potential difference (CPD) between CdSe and AFM probe, and work-function (WF) was calculated using the formula: $CPD = (WF_{sample} - WF_{tip})/e$, with gold as a reference sample with a known work-function and "*e*" being the electronic charge. CPD was calculated to be at 32.8 and 111 mV for CdSe3.7 and CdSe5.0, respectively. Using these values and the gold work function (5.1 eV) as a reference, the WF of CdSe3.7 and CdSe5.0 was calculated to be at 5.0 and 5.10 eV, respectively.

To measure the valence-band maximum (VBM), vacuum ultraviolet photoelectron spectroscopy with 80 eV photon energy was carried out. The low binding energy (BE) side of the valence band spectrum depicts the energy difference between the valence-band edge of QDs and the Fermi-level of gold from which VBM is obtained. The rising edges of the valence band in the plot are at 1.55 and 1.7 eV for CdSe3.7 and CdSe5.0, respectively, from the Fermi-level of gold ($E_f = 0$), as shown in SI, section S7, Figure S8(a),(b). Combining both work-functions from KPFM and BE from UPS, the valence-band maximum (VBM) for CdSe3.7 and CdSe5.0 is at 6.55 and 6.80 eV, respectively, and are closer to bulk CdSe valence band maximum, thus, demonstrating an energetically favorable hole-transfer at the interface of the CQDs with *a*-Se. The CBM for both CdSe3.7 and CdSe5.0 was obtained by adding the optical bandgap with the VBM. As shown in Figure 2c and SI, section S7, Figure S8(c), we represent the band-edge alignment at the interface between CdSe3.7, CdSe5.0, and *a*-Se[30] representing the energy barrier for electron-transfer and the energetically favorable hole-transfer.

While PL quenching experiments coupled with valence band offsets between CdSe and *a*-Se indicated energetically favorable photogenerated hole-transfer from CdSe to *a*-Se, we utilized KPFM to validate the type of charge-transfer and band offset.[24,31] In order to determine the direction of charge-transfer, electron−hole pairs were created by illuminating the surface of the CdSe layer using green LEDs (peak at 515−525 nm). Figure 2d is a schematic representation of the expected decrease in CPD upon illumination with green light. Since WF of CdSe/*a*-Se is lower than KPFM tip (inferred from measured negative $CPD = (WF_{sample} - WF_{tip})/e$), the induced charges are positive on CdSe/*a*-Se side and negative near the tip during equilibration. Illumination of the surface creates electron−hole pairs and if the holes are transferred into *a*-Se layer, the remaining negative charges compensate for the induced positive charge at the surface and thus reduce the absolute value of CPD measured in dark, as shown in the inset of Figure 2d. The surface potential maps for the measurements conducted in dark and upon illumination are shown in Figure S7(c)−(j) along with the topography of the samples measured and the respective plots of CPD are shown in Figure 2e and f. Following illumination, there is a saturation of surface potential as shown in Figure 2e, representing the final equilibrium stage of the quasi-Fermi-levels of both semiconductors (CdSe and *a*-Se). As seen from Figure 2f, the CPD in the dark is −604 mV, and −783 mV for CdSe3.7 and CdSe5.0, respectively. After illumination, the surface potentials shift to lower negative values of −532 and −642 mV for CdSe3.7/*a*-Se and CdSe5.0/*a*-Se, respectively, indicating the hole-transfer at the CdSe/*a*-Se interface. Thus, a combination of PL emission quenching and photoresponse measurement in KPFM proves that *a*-Se is an efficient HTL for CdSe CQDs. The type-II heterojunction formed between *a*-Se acting as a reliable hole transport medium coupled to a solution-processed quantum dot photoactive layer capable of absorbing light in the visible part of the electromagnetic spectrum has potential to be extended to short and mid-IR regions of the electromagnetic spectrum. Next, we show the electrical characterization results for the CdSe/*a*-Se hybrid photodetector.

The J_D characteristics as a function of electric field across the *a*-Se layer, as shown in Figure 3a, were measured for CdSe3.7/*a*-Se, CdSe5.0/*a*-Se, and CdSe5.0/*a*-Se with CeO_2 HBL detector samples. The electric field across individual materials in the detector as a function of applied bias is simulated in SIsection S8.1, Figure S9. The steady-state J_D for the CdSe3.7/*a*-Se and CdSe5.0/*a*-Se detectors without a HBL, was measured to be in the order of $\sim nAcm^{-2}$ corresponding to 40 V/μm applied electric field across the *a*-Se layer. Due to the large electronic bandgap of the materials used in the detector (see SI, section S2 and Table S1), the thermally generated carriers in the intrinsic region of the detector do not contribute to the measured J_D. Under light starved conditions, the dominant source limiting J_D in *a*-Se based detectors is Schottky or thermionic hole injection from the high voltage ITO electrode.[20] Thus, we observe even lower levels of J_D in Figure 3a for the CdSe5.0/*a*-Se detector with an added CeO_2 CQD HBL with an enhanced bandgap of ∼3.77 eV. The high-k CeO_2 (ranging between 24 and 52) noninsulating blocking layer substantially decreases the electric field at the blocking-layer/metal−electrode interface, limits the Schottky injection from the electrodes, prevents Joule heating from crystallizing the *a*-Se layer, hinders the irreversible breakdown of the device, and enables maximum extraction of photogenerated carriers.[20]

Carriers once injected into the detector must travel across the detector material system to recombine at the ITO electrodes. Based on the similarity in terms of hopping transport via localized states between disordered organic solids (molecularly doped polymers) and chalcogenide glasses (*a*-Se and As_2Se_3), the DDOS distribution and other activated transport mobility models were incorporated in the simulation, see SIsection S8.2. Figure 3a also shows the simulation results for J_D, validated with experimentally measured values for the CdSe5.0/*a*-Se device with a CeO_2 HBL. Moreover, the device J_D performance is not significantly improved with the use of a higher work-function bottom electrode (see SI, section S8.3 and Figure S12).[12,20] To investigate the dependence of J_D on the thickness of the *a*-Se, we simulate four *a*-Se layer thicknesses: 1, 5, 10, and 15 μm, as shown in SIsection S8.4. From Figure S13, we observe an insignificant dependence of the bulk *a*-Se thickness on the overall J_D due to negligible thermal generation of carriers in the wide-bandgap *a*-Se layer.

https://doi.org/10.1021/acsphotonics.2c01353
ACS Photonics 2023, 10, 134−146

To experimentally show the weak dependence of J_D on the thickness of *a*-Se, we fabricated two control *n*−*i* detectors with 5 and 10 μm *a*-Se, respectively. A detailed description of the measured J_D results is shown in SI, section 9.1 and Figure S14. From the figure, we observe that irrespective of the thickness of the *a*-Se layer, the J_D as a function of the electric field for both the 5 and 10 μm *a*-Se devices are in the same ballpark. Measured J_D transients for the CdSe5.0/*a*-Se detector with a CeO_2 HBL is shown in SI, section S9.2 and Figure S15. Using TCAD simulations and experiments, we came to the conclusion that the J_D in our detector structure does not scale by decreasing the *a*-Se thickness, thus allowing our detectors operated at high bias voltages (see Figure S9) to be scaled down by the thickness of the *a*-Se HTL (15 μm in the manuscript). Although, commercial *a*-Se X-ray indirect conversion detectors are biased at voltages beyond 2000 V, with the readout being operated between 10 and 20 V, for other applications, the detector can be operated at smaller applied biases by shrinking the 15 μm *a*-Se layer thickness.[14]

EQE results for CdSe3.7/*a*-Se and CdSe5.0/*a*-Se with CeO_2 HBL are shown in Figure 3b. The EQE increases with an increase in an electric field. The generation of bound electron−hole pairs (excitons) and their subsequent dissociation into free charge carriers are the two important factors that directly impact the light-harvesting efficiency of the semiconductor quantum dots. The dissociation of excitons is a complex process that is influenced by various factors such as the shape and size of the quantum dots, the presence of surface defects, surface ligands, and coupling with phonon modes. At a certain electric field, the quantum efficiency decreases with an increase in the wavelength of incident light. Figure 3b also shows the simulation results for the CdSe5.0/*a*-Se with CeO_2 HBL detector: see SI, sections S10.1 and S10.2 for a complete description on photoresponse modeling using TCAD. To further explain the underestimation of the TCAD simulated EQE with experiment at low electric fields for the CdSe5.0/*a*-Se with CeO_2 HBL detector structure, in Figure 3b, we calculate the transmission probabilities obtained from solving the 1D Schrödinger wave equation along paths perpendicular to the CQD interface by using an N barrier one-dimensional piecewise constant potential barrier tool (N-PCPBT). Further details regarding the N-PCPBT simulation framework are provided in SI, section S10.3. Our measured EQE of ∼26% for the CdSe5.0/*a*-Se with CeO_2 HBL detector is the highest efficiency measured for a CdSe CQD based photodiode (previously 200 nm CdSe CQD based device with measured EQE ∼ 8−10%)[33] in the spectrum window of 500−550 nm. The CdSe layer absorbs the majority of the incoming photons, while the remaining are absorbed in the *a*-Se layer. Figure 3b also shows the measured and TCAD simulated EQE results in a fabricated control sample without the CdSe CQD layer, where *a*-Se acts as the only photon-absorption layer (shown by hollow circular marker). From Figure 3b, the control sample EQE for *a*-Se decreases from ∼80% to less than 1%, as the wavelength of excitation light increases from 405 to 656 nm. respectively. SI, section S11.2, and Table 1 separate the individual contributions on EQE from the CdSe5.0 CQD and the *a*-Se layer, respectively. From Table 1 we can see that the majority of the contribution to EQE is from the CdSe5.0 CQD layer with the *a*-Se layer acting as an efficient HTL, see SI, section S11.2. SI, section S11.3 and Figure S24 show the measured responsivity (A/W) for blue (405 nm), green (530 nm), and red (656 nm) light in the *p*-*i*-*n* CdSe3.7/*a*-Se and CdSe5.0/*a*-Se with CeO_2 HBL detector structures. Figure 3c compares the simulated singlet exciton activation energy with experimentally reported values for the CdSe5.0 CQD layer.[36] The activation energy range of 0.205−0.22 eV simulated using our model for 5.0 nm CdSe dot size is a close match to the previously reported value of ∼0.225 eV for 4.8 nm CdSe CQD size.[36] It has been previously reported that enhancement of the exciton dissociation process can be obtained by increasing the CQD size resulting in a decrease in exciton recombination probability.[36] Thus, we also observe an increase in EQE, as the CQD size increases from 3.7 to 5 nm.

Table 1. EQE for CdSe5.0/*a*-Se with CeO_2 CQD HBL Detector Structure with Individual Contributions from the CdSe5.0 Layer and the *a*-Se Layer at Different Electric Fields

electric field	EQE device, %			EQE *a*-Se, %			EQE CdSe5.0, %		
V/μm	blue	green	red	blue	green	red	blue	green	red
10	29	7	1.5	12	1	0	17	6	1.5
20	41	13	2	15	2	0	26	11	2
30	50	19	2.5	17	3	0	33	16	2.5
40	55	26	2.5	18	4	0	37	22	2.5

Linear dynamic range is a figure-of-merit for photodetectors to characterize the light intensity range in which the photodetectors have a constant responsivity. Beyond this range, the intensity of the light signal cannot be detected and calculated precisely. LDR is given by

$$\mathrm{LDR} = 20 \times \log\left(\frac{J_{ph}}{J_d}\right)$$

where J_{ph} is the photocurrent measured at a light intensity of 1 mW cm^{-2}.[37] The LDR measured as a function of electric field across the *a*-Se layer is shown in Figure 3d. From Figure 3d, the measured LDR was ∼145 and 135 dB for blue (405 nm) and green (530 nm) excitation light wavelengths, respectively.

Figure 4a shows the measured ultralow noise current of the CdSe5.0/*a*-Se with CeO_2 detector, which is in the order of ∼20 fA/$Hz^{1/2}$. The shot noise limited approximation of noise current, which is in the order of ∼1 fA/$Hz^{1/2}$, is represented by the dashed line in Figure 4a. The frequency dependence of the noise current and its attainment to a steady state value beyond 1 kHz is shown in SI, section S12.1 and Figure S25, at 30 V/μm. Note that the noise measurements up to 250 Hz were affected by the microphonics in the measurement room, as marked by the red box in Figure S25. This steady-state noise current measured away from the microphonics of the measurement setup is an order of magnitude higher than the shot noise approximation and can be attributed to thermal and generation-recombination noise.[10] Based on the measured noise current from Figure 4a and the responsivity (R) of the devices (see Figure S24), the noise equivalent power (NEP = i_n/R) of the device at 40 V/μm is calculated as shown in Figure 4b (see SI, section S12.2 and Figure S26 for more details). The NEP expresses the minimum detectable power per square root bandwidth of a given detector; in other words, it is a measure of the weakest optical signal that can be detected. The measured NEP in Figure 4b increases as a function of increasing wavelength because of the decrease in device responsivity/EQE as the excitation light wavelength increases. To compare photodetectors with the different active areas, the

https://doi.org/10.1021/acsphotonics.2c01353
ACS Photonics 2023, 10, 134−146

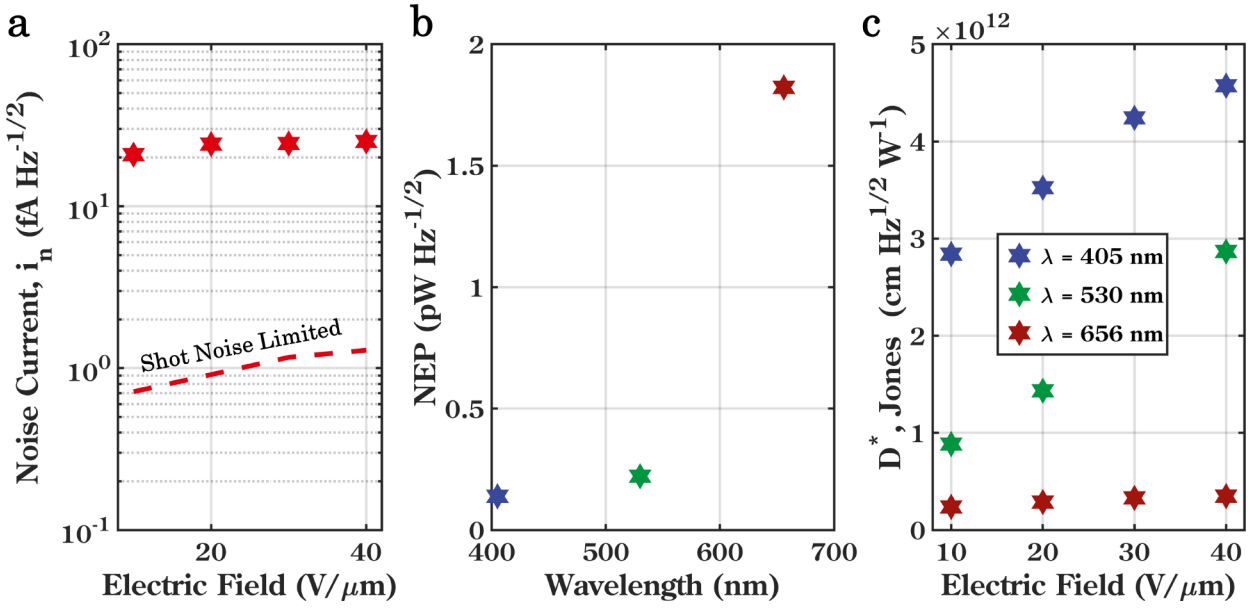

Figure 4. Measured (a) noise current (fA/Hz$^{1/2}$), (b) noise equavalent power (pW/Hz$^{1/2}$) at 40 V/μm, and (c) specific detectivity (Jones) in the CdSe5.0/*a*-Se structures with CeO_2 CQD HBL. All device measurements were performed at room temperature (295 K).

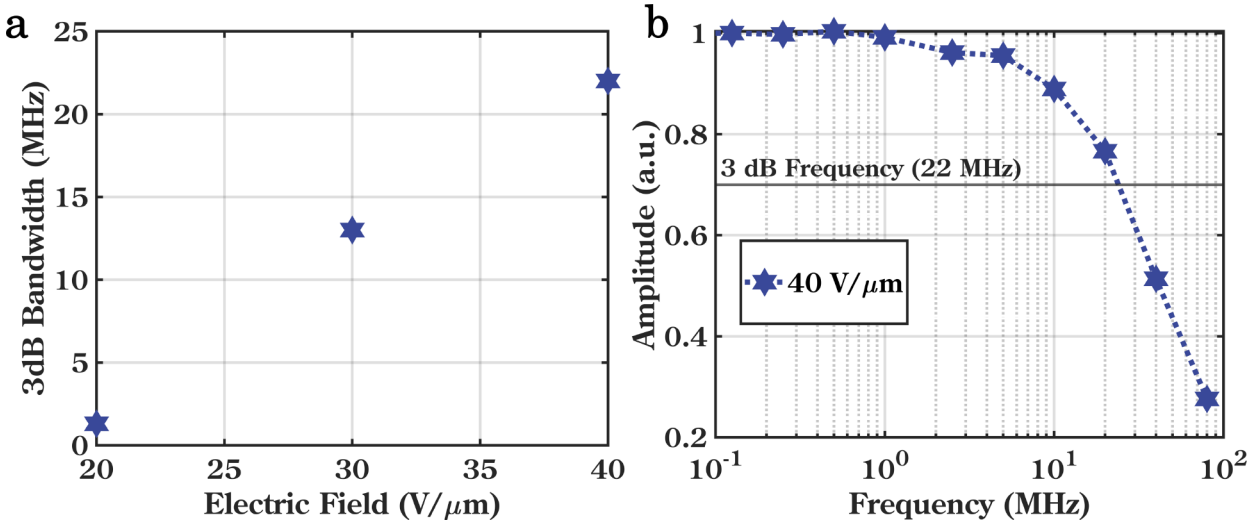

Figure 5. Temporal characterization of *a*-Se/CdSe devices with HBL. (a) Measured 3 dB bandwidth as a function of applied electric field. (b) Measured normalized photocurrent as a function of frequency 40 V/μm. All device measurements were performed at room temperature (295 K).

device's active area should be considered. We have measured high specific detectivity in the order of ~5 × 10 ^{12} Jones, as shown in Figure 4c. Our measured device specific detectivity is comparable to state-of-the-art commercial Si PD (~4 × 10 ^{12}),[38] PbS PD (~5 × 10 ^{12}),[34] PbS PC (~10^{13}),[39] and perovskites (PVK)-based PVK:Zr:TiO_x (~10^{13}) detectors.[40] The specific detectivity is expressed as $D = \frac{(Af)^{1/2}}{R/i_n}$), where A is the effective area of the detector, f is the electrical bandwidth, R is the responsivity, and i_n is the noise current. In Figure 4c, higher electric fields allow for enhanced photogenerated charge extraction, leading to an increase in device detectivity. Beyond 40 V/μm, the device encountered a soft breakdown localized and randomly distributed all over the device area. It is worth pointing out that our measured detectivity values (Figure 4(c)) are not based on a shot noise limited current approximation which would otherwise overestimate the detectivity values by an order of magnitude.

We next characterize temporal performance of our fabricated *p*−*i*−*n* vertical stack detector. For the best performing CdSe5.0/*a*-Se device with a CeO_2 HBL, the 3 dB cutoff frequency was measured using a 405 nm laser source. The 3 dB modulation frequency at which the responsivity is $1/\sqrt{2}$ of that obtained under continuous illumination was measured as a function of the electric field, as shown in Figure 5a. At 40 V/μm the 3 dB bandwidth was measured to be ~22 MHz, as shown in Figure 5b. The speed of our CQD detector represents a 400% improvement in 3 dB bandwidth response speed over the most sensitive CQD photodetector reported.[34] The 3 dB BW can also be approximated using the rise time (the time it take for the detector signal to equal to 63% of its steady state value) as BW = 0.35/t_r, where t_r is the rise time of the transient photocurrent pulse. The 3 dB bandwidth value of

https://doi.org/10.1021/acsphotonics.2c01353
ACS Photonics 2023, 10, 134−146

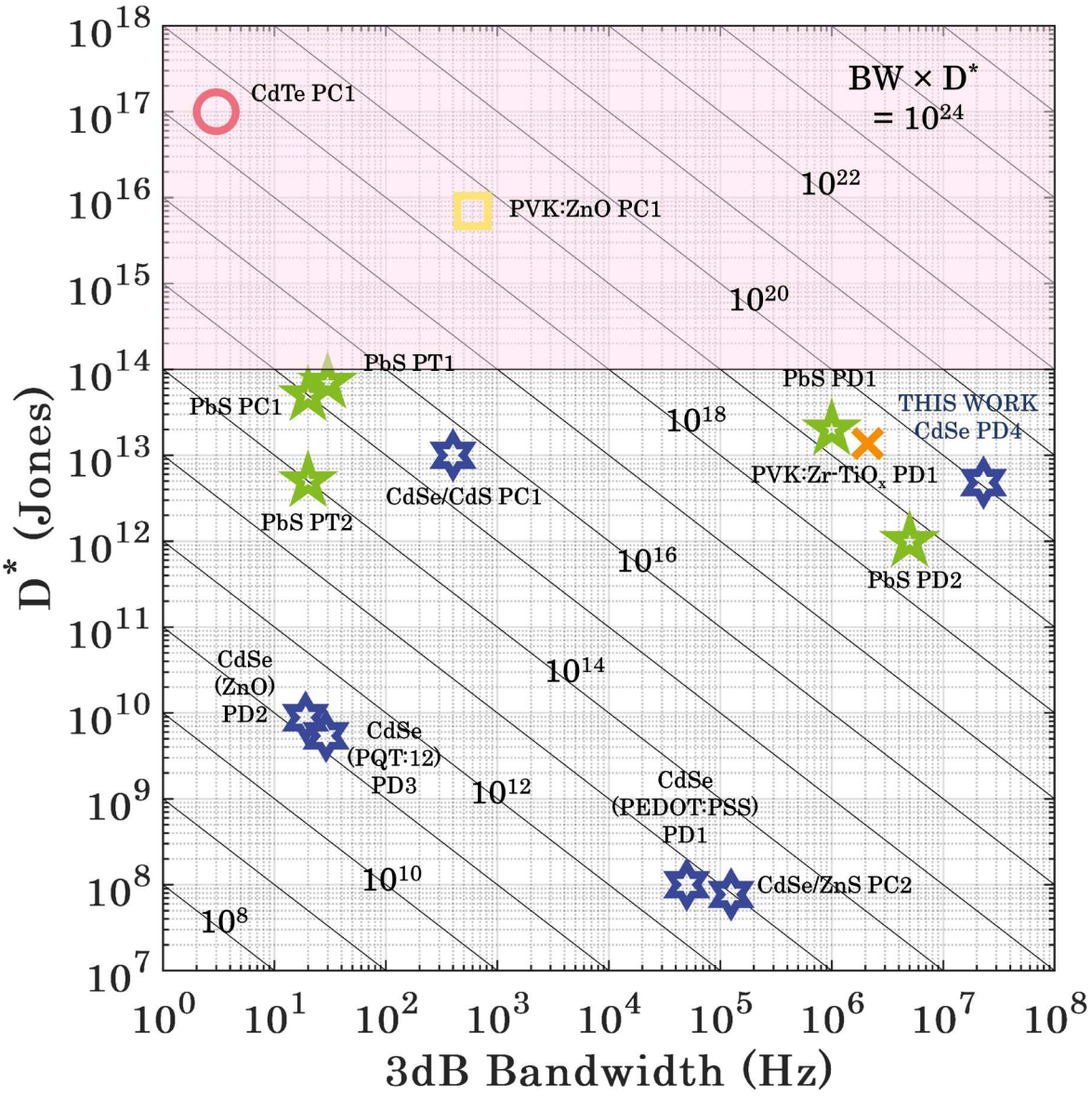

Figure 6. Measured detectivity-bandwidth product comparison for state-of-the-art solution-processed thin-film photodetectors. CdSe solution-processed detectors are shown using blue hexagram markers: CdSe/CdS PC1,[41] CdSe/ZnS PC2,[42] CdSe w. PEDOT:PSS PD1,[33] CdSe w. ZnO PD2,[43] CdSe w. PQT:12 PD3,[44] and this work CdSe PD4. PbS solution-processed detectors are shown using green pentagram markers: PbS PT1,[45] PbS PT2,[46] PbS PC1,[39] PbS PD1,[47] and PbS PD2.[34] Perovskite (PVK)-based detectors are shown as PVK:Zr:TiO_x.[40] CdTe PC1 and PVK:ZnO PC1 detectors show ultrahigh detectivity based on a high internal gain.[11,48]

Table 2. Comparison of the CdSe5.0/*a*-Se with CeO_2 HBL Detector with State of the Art CdSe-Based CQD Detectors with/without TLs

photoactive CQD material	orientation/type	structure	D^* (Jones)	3 dBBW/rise time (RT)	gain/R(A/W)
CdSe5.0(this work)	vertical PD	ITO/As_2Se_3/*a*-Se/CdSe/CeO_2/ITO	~5 × 10^{12}	22 MHz	G = 1
CdSe[10,33]	vertical PD	ITO/PEDOT:PSS/CdSe/Ag	~10^8	50 kHz	G = 1
CdSe[43]	vertical PD	*n*-Si/ZnO/CdSe/Au	~8.8 × 10^9	19 Hz(RT = 17.9 ms)	G = 1
CdSe[44]	vertical PD	ITO/PQT-12/CdSe/Au	~5.4 × 10^9	29 Hz(RT = 12.01 ms)	G = 1
CdSe/CdS[41]	vertical PC	Al/CdSe(CdS)/ITO	~10^{13}	0.4 kHz	$G \gg$ 1/260A/W
CdSe NWs[49,50]	lateral PC	Au/CdSe/Au	3.77 × 10^9	44 kHz	$G \sim$ 5
CdSe NWs[49,50]	lateral PC	Au/CdSe/Au	4.4 × 10^{10}	43 mHz	G = 0.017
CdSe/ZnS[42] core−shell QDs	lateral PC	Au/CdSe/Cr	7.1 × 10^7	125 kHz	5.88 mA/W
CdSe nanogap[50] core−shell QDs	lateral PC	Au/CdSe/Au	6.9 × 10^{10}	175 kHz	$G \sim$ 45

1.27 MHz, measured at 20 V/μm, calculated using the t_r (as shown in SI, section S13 and Figure S27) is a close approximation to that measured using the pulsed laser technique: 3 dB bandwidth ~ 1.3 MHz at 20 V/μm. The dark and photo current stability of the photon absorbing CdSe5.0 layer was investigated by measuring the dark and

https://doi.org/10.1021/acsphotonics.2c01353
ACS Photonics 2023, 10, 134−146

photon response of the detector over a period of 25 days. SI, section S14.1 and Figure S28, shows the normalized dark and photon response of the detector as a function of time, measured at an applied bias of 600 V. The CdSe5.0 CQD layer shows minimal degradation in electrical performance over the time period of 25 days. In order to investigate the temporal stability of the detector, we illuminated the detector with 200, 20 ms pulses with a duty cycle of 50% at a bias voltage of 340 V, corresponding to an electric field of 20 V/μm across the *a*-Se layer. From SI, section S14.2 and Figure S29, we observe that there is no residual signal on subsequent exposures and the peak of the output pulses remain approximately constant over time for blue (405 nm) and green (530 nm) light, respectively. It is evident that the temporal characteristics of this CQD based heterostructure is excellent and provides a path toward scaling up as an imager.

In Figure 6, we compare our detectivity and bandwidth with measured current state-of-the-art designs for different material classes. Until now, PQT-12, ZnO, and PEDOT:PSS have been explored as transport layers for CdSe CQDs, as shown in Table 2 and Figure 6.[33,43,44] In Figure 6, the solid black lines represent the detectivity-bandwidth product equipollent lines. Our hybrid CdSe/*a*-Se devices demonstrate the highest measured detectivity-bandwidth product ~10^{20} Jones × Hz, a 500% improvement than the current state-of-the-art: PVK:Zr:TiO_x,[40] and PbS PD1,[47] and an improvement by over 4 orders of magnitude than the current state-of-the-art: CdSe CQD based detector.[41]

CONCLUSIONS

In summary, this work reports a proof-of-concept for fabricating vertical-stack-photodetectors using a facile, low-cost, and room-temperature solution-processed CdSe CQD photoconversion layer coupled to *a*-Se as a HTL in the desired *p*−*i*−*n* fabrication sequence, which has the potential to be fabricated as an imager. We report ultralow J_D ~ 10 pAcm^{-2}, high linear dynamic range ~ 150 dB, high specific detectivity ~ 5 × 10 ^{12} Jones, and fast temporal response ~ 22 MHz, which is 3 orders of magnitude higher than previously reported CdSe photodetectors detectivity and 400 times higher bandwidth than previously reported CdSe PDs. Dark and photon response of the detector was further validated using TCAD simulations decoupled to a N-PCPBT Schrödinger solver. Our simulations confirm that the main source of dark current in *a*-Se detectors is the injection of holes from the high-voltage electrode. Thus, a solution-processed high-k CeO_2 CQD HBL, with enhanced hole blocking due to quantum confinement effects, was added to suppress the electric field near the high-voltage electrode, resulting in a significant reduction in injected carriers from Schottky emission. Currently, we are investigating ultrahigh-k CQDs (e.g., $SrTiO_3$, and $BaTiO_3$) as potential HBLs in *a*-Se based avalanche photodetectors. The results show that majority of the observed EQE is from the CdSe layer with *a*-Se predominantly acting as an efficient HTL. Although the device broke down prior to avalanche, the type-II heterojunction formed between *a*-Se and CdSe shows an improvement by over 4 orders of magnitude in the detectivity-bandwidth product than the current state-of-the-art: CdSe CQD-based detector. Furthermore, with PL-emission quenching and KPFM measurements, we demonstrate that *a*-Se acts as an extremely efficient HTL for CdSe CQD-based photodetectors and holds the capability to develop high-speed photodetectors in the visible part of the electromagnetic spectrum with potential to be coupled to IR responsive CQDs. In the future, avalanche multiplication can be obtained in this coupled vertical structure by using a parametrically optimized set of device layer thicknesses, exploring an effective ligand selection and exchange to enhance transport in the CQD film, and help sustain higher electric fields, and designing devices with nano-Frisch grids to operate the CQD layer at low electric fields while operating the *a*-Se layer at an electric field beyond the onset of impact ionization avalanche.

METHODS

Solution Synthesis. All chemicals (see SI, section S15) were used as purchased without any further purification. CdSe CQDs were synthesized using a modified procedure by Kang et al.[22] 822 mg of CdO, 16.4 g of TOPO, 37 g of HDA, and 3.415 g of DDPA were combined in a 250 mL four-neck round-bottom flask. The added reactants were heated to 90 °C with a stirring rate at 1000 rpm to melt all the reactants. At this temperature, the mixture was degassed three times to below 0.5 Torr. Following the degassing, the temperature was raised to 320 °C and maintained until the solution turned colorless. The temperature was set at 280 °C for CdSe3.7 CQDs, and 40 mL of 0.2 M TOP:Se with 0.6 mL of DPP was added. To achieve CdSe5.0 CQDs, the temperature was set at 260 °C, and 40 mL of 0.2 M TOP:Se without DPP was added and the particles were grown until the absorption at 620 nm was reached. The reaction was subsequently air-cooled, and the flask was submerged in a water bath at 200 °C. A total of 40 mL of 1-butanol was added to the mixture at 130 °C to prevent solidification of the reaction mixture. Methanol was added to the above mixture in the centrifuge tube and centrifuged at 4000 rpm for 10 min and the supernatant was discarded. Hexane was added to the above sediment, the mixture was vortexed and left undisturbed overnight. The next day, the mixture was centrifuged at 4000 rpm for 20 min. The precipitates were discarded and the colored supernatant was added with reagent alcohol until the solution turned turbid. Further, the mixture was centrifuged at 4000 rpm for 10 min and the clear supernatant was discarded. The cleaning procedure was repeated three times to obtain pure CdSe nanocrystals and were stored in an inert atmosphere. CdSe QDs were prepared in a hexane to octane ratio of 8:2 to form 30 mg/mL. For absorption studies, CdSe CQDs were dispersed in hexane, and the measurement was carried out in Agilent Cary5000 UV−vis-NIR spectroscopy with a spectral bandwidth of 2 nm and was operated in the transmission mode.

CeO_2 colloidal QDs for the hole-blocking layer were synthesized using a modified procedure proposed by Runnerstrom et al. and was reported in our previous literature.[12] Cerium(III) nitrate hexahydrate ($Ce(NO_3)_3 \cdot 6H_2O$) was taken as the precursor that undergoes decomposition at 250 °C, followed by nucleation and growth of the nanocrystals. As-synthesized QDs were dispersed in a solvent ratio of hexane and octane of 8:2 to form 30 mg/mL colloidal dispersions for further use in thin film fabrication.

Thin-Film Fabrication. The solution-processed CdSe QDs were spun-coat on *a*-Se layer. All the solutions were prepared at 30 mg/mL. CdSe3.7 and CdSe5.0 were spun-coat at 2400 rpm and 45 s. Assembled CdSe QD films were ligand exchanged with 130 mM (1%w/v) solution of ammonium thiocyanate (NH_4SCN) in acetone at 2400 rpm and 35 s, followed by spin coating of pure acetone with the spin

https://doi.org/10.1021/acsphotonics.2c01353
ACS Photonics 2023, 10, 134−146

parameters of 2400 rpm and 30 s, to remove any unbound NH_4SCN. This process was continued until the required thickness was achieved. For the deposition of the hole-blocking layer, CeO_2 of 30 mg/mL was spin-coated at 2000 rpm, 45 s, followed by ligand exchange solution of ammonium thiocyanate in acetone and cleaning solvent (acetone) at the same spin-coating parameters.

Device Fabrication. Each avalanche device utilized a *p-i-n* fabrication process developed on 2.5 × 2.5 in^2 Borofloat glass substrates, coated with 75 nm ITO. This bottom ITO layer functions as one large, common readout electrode. The *p*-layer and *a*-Se *i*-layer was thermally evaporated through a shadow mask with a 5.5 cm × 5.5 cm opening. The *p*-layer consisted of a 2 μm thermally evaporated inorganic electron blocking layer, followed by the thermal evaporation of stabilized vitreous selenium pellets, forming the 15 μm *a*-Se *i*-layer. Each wafer had four total HV 50 nm ITO electrodes deposited, all of an equal area ∼ 0.4 cm^2. Transparent ITO HV electrodes were patterned by a shadow mask and deposited via electron beam deposition.

Dark and Photoconductivity Measurement. The detector was illuminated through the top ITO transparent contact. Mightex's PLS- series precision LED light source was used to provide uniform and high-intensity illumination. For each measurement, a CAEN N1471A programmable high voltage power supply was used to positively bias the top electrode of the devices. The time- (I−t) and voltage (I−V)-dependent photo/dark current characteristics were measured with a Keithley 6514 electrometer. The irradiance was calibrated using a Thorlabs PM400 optical power and energy meter placed at the position of the CQD photodiode. All measurements were performed in a dark, shielded enclosure at room temperature (295 K) in air. For transient photocurrent measurements, a Seoul Semiconductor Inc. Z power series LED was used with a Tektronix AFG 3021B function generator with 170 ns fwhm used to supply a modulated bias to the LEDs. The induced photocurrent was captured by a Teledyne LeCroy 640ZI 4 GHz digital oscilloscope. Tektronix P6245 active probes with a 1 MΩ input resistance were used to protect the oscilloscope against device failure at high *F*s and create a charge integrating circuit. For all photocurrent measurements, the *a*-Se devices were mounted in a light tight, grounded metal box. The signal current from a single LED pulse was used to evaluate the effective quantum efficiency at each applied field. Prior to exposure, the target HV bias was held for several seconds. After each measurement, the HV bias was ramped down to 0 V and the light tight box was opened to depolarize the sample. The dark current was subtracted from each measured signal current to mitigate offset in the photogenerated charge.

3 dB Measurement. The temporal response is typically characterized by the 3 dB bandwidth was measured using a 405 nm picosecond PicoQuant Laser source. The frequency of the laser is doubled for each measurement which doubled the power contained in each laser pulse. The current was measured with a Keithley 6514 electrometer and normalized for the doubling in power. The 3 dB bandwidth was measured as the frequency at which, the normalized photocurrent is 0.7 times that of its steady state value.

Noise Current Measurement. Noise current was directly measured with a lock-in amplifier SR865A. The photodetectors were kept in the dark room and shielded in a light-tight box. A Faraday shield was constructed using Al foil to prevent interference from microphonics. The SR865A lock-in-amplifier was operated in current mode. Noise current was measured in units of $A/Hz^{1/2}$.

Detector Modeling. TCAD level device simulations was performed using the Silvaco, ATLAS simulation framework. The electric field across the different layers of the detectors as a function of applied external bias and the validation of experimentally observed dark and photoresponse of the CdSe5.0/*a*-Se detector was also performed using TCAD simulations decoupled to an N barrier one-dimensional piecewise linear potential barrier (N-PCPBT) Schrödinger solver. Detailed information on TCAD models and current conduction mechanisms incorporated, and dark and photocurrent modeling is provided as separate chapters in the Supporting Information.

■ ASSOCIATED CONTENT

Supporting Information

The Supporting Information is available free of charge at https://pubs.acs.org/doi/10.1021/acsphotonics.2c01353.

> Further details on the low noise phenomenology in *a*-Se thin-films, the TCAD simulation framework, structural and optical characterization, photoluminescence quenching measurement details, bulk CdSe band edges, Kelvin probe microscopy results, ultraviolet-photoelectron spectroscopy results, simulation details of dark current, supporting dark current measurement results, simulation details on photoresponse, further measurement details on photoresponse, noise current, noise equivalent power, 3 dB bandwidth, and device stability (PDF)

■ AUTHOR INFORMATION

Corresponding Authors

Ayaskanta Sahu − *Department of Chemical and Biomolecular Engineering, Tandon School of Engineering, New York University, Brooklyn, New York 10012-1126, United States;* orcid.org/0000-0002-1508-0213; Email: asahu@nyu.edu

Amir H. Goldan − *Department of Radiology, School of Medicine, Stony Brook University, Stony Brook, New York 11794, United States*; Email: amirhossein.goldan@stonybrookmedicine.edu

Authors

Atreyo Mukherjee − *Department of Electrical Engineering, College of Engineering and Applied Sciences, Stony Brook University, Stony Brook, New York 11794, United States;* orcid.org/0000-0002-8451-7167

Haripriya Kannan − *Department of Chemical and Biomolecular Engineering, Tandon School of Engineering, New York University, Brooklyn, New York 10012-1126, United States*

Le Thanh Triet Ho − *Department of Electrical Engineering, College of Engineering and Applied Sciences, Stony Brook University, Stony Brook, New York 11794, United States;* orcid.org/0000-0003-4984-467X

Zhihang Han − *Department of Electrical Engineering, College of Engineering and Applied Sciences, Stony Brook University, Stony Brook, New York 11794, United States*

https://doi.org/10.1021/acsphotonics.2c01353
ACS Photonics 2023, 10, 134−146

Jann Stavro − *Department of Radiology, School of Medicine, Stony Brook University, Stony Brook, New York 11794, United States*
Adrian Howansky − *Department of Radiology, School of Medicine, Stony Brook University, Stony Brook, New York 11794, United States*
Neha Nooman − *Department of Electrical Engineering, College of Engineering and Applied Sciences, Stony Brook University, Stony Brook, New York 11794, United States*
Kim Kisslinger − *Center for Functional Nanomaterials, Brookhaven National Laboratory, Upton, New York 11973, United States*
Sébastien Léveillé − *Analogic Canada, Montreal, QC H4R 2P1, Canada*
Orhan Kizilkaya − *Center for Advanced Microstructures and Devices, Louisiana State University, Baton Rouge, Louisiana 70803, United States*
Xiangyu Liu − *Department of Chemical and Biomolecular Engineering, Tandon School of Engineering, New York University, Brooklyn, New York 10012-1126, United States;* orcid.org/0000-0001-7010-6554
Håvard Mølnås − *Department of Chemical and Biomolecular Engineering, Tandon School of Engineering, New York University, Brooklyn, New York 10012-1126, United States*
Shlok Joseph Paul − *Department of Chemical and Biomolecular Engineering, Tandon School of Engineering, New York University, Brooklyn, New York 10012-1126, United States*
Dong Hyun Sung − *Department of Chemical and Biomolecular Engineering, Tandon School of Engineering, New York University, Brooklyn, New York 10012-1126, United States*
Elisa Riedo − *Department of Chemical and Biomolecular Engineering, Tandon School of Engineering, New York University, Brooklyn, New York 10012-1126, United States*
Abdul Rumaiz − *National Synchrotron Light Source II, Brookhaven National Laboratory, Upton, New York 11973, United States*
Dragica Vasileska − *School of Electrical, Computer and Energy Engineering, Arizona State University, Tempe, Arizona 85287, United States*
Wei Zhao − *Department of Radiology, School of Medicine, Stony Brook University, Stony Brook, New York 11794, United States*

Complete contact information is available at: https://pubs.acs.org/10.1021/acsphotonics.2c01353

Author Contributions

†The authors A.M. and H.K. contributed equally to this work and are first authors.

Author Contributions

A.H.G., W.Z., and A.S. designed the devices. H.K., O.K., X.L., D.S., E.R., and A.S. synthesized, characterized, and deposited the QDs. S.L. deposited *a*-Se. K.K. did the FIB-TEM of the device structure. A.M. and A.H.G. designed the experiments. A.M., A.H.G., N.N., J.S., A.R., A.H., and Z.H. conducted the electrical characterization of the device. A.M., D.V., and A.H.G. devised the simulation framework, and A.M. and L.T.T.H. obtained modeling results. A.M., H.K., A.S., and A.H.G. analyzed the data and wrote the manuscript. A.H.G. and A.S. supervised the research. All the authors discussed the obtained results and proofread the manuscript.

Funding

We gratefully acknowledge financial support from the National Institutes of Health (R21 EB025300). The author A.H.G. acknowledges the financial support from the National Science Foundation (ECCS 2048390). The author D.V. also acknowledges the financial support from the National Science Foundation (ECCS2025490 and ECCS 2048400). We thank the support to the X-ray facility by the National Science Foundation under Award Number CRIF/CHE-0840277 and by the NSF MRSEC Program under Award Numbers DMR-0820341 and DMR-1420073. Kelvin-Probe Force Microscopy work by the authors X.L. and E.R. acknowledge support from the U.S. Department of Energy, Office of Science, Basic Energy Sciences, MSE Division under Award # DE-SC0018924 and U.S. Army Research Office under Award # W911NF2020116.

Notes

The authors declare the following competing financial interest(s): A.H.G., A.S., W.Z., A.M., and H.K. have filed a provisional patent application 63/270,773 based on the results of this manuscript.

■ ACKNOWLEDGMENTS

The authors acknowledge Research Computing at Arizona State University for providing (HPC, storage, etc.) resources that have contributed to the research results reported in this paper. The author D.V. gratefully acknowledges the academic donation of Silvaco TCAD tools by Silvaco Inc. used in this study. Work by the author H.K. was (partially) supported by the Schlumberger Foundation Faculty for the Future Program. The author(s) would like to acknowledge the Imaging Facility of CUNY Advanced Science Research Center for instrument use and scientific and technical assistance. We thank Prof. Eray Aydil from NYU, Department of Chemical and Biomolecular Engineering, for helping us to conduct photoluminescence measurements in Horiba Scientific Quanta Master and Quanta-ϕ.

■ REFERENCES

(1) Dong, Y.; Wang, Y.-K.; Yuan, F.; Johnston, A.; Liu, Y.; Ma, D.; Choi, M.-J.; Chen, B.; Chekini, M.; Baek, S.-W.; et al. Bipolar-shell resurfacing for blue LEDs based on strongly confined perovskite quantum dots. *Nat. Nanotechnol.* **2020**, *15*, 668−674.
(2) Park, Y.-S.; Roh, J.; Diroll, B. T.; Schaller, R. D.; Klimov, V. I. Colloidal quantum dot lasers. *Nat. Rev. Mater.* **2021**, *6*, 382−401.
(3) Bernechea, M.; Cates, N.; Xercavins, G.; So, D.; Stavrinadis, A.; Konstantatos, G. Solution-processed solar cells based on environmentally friendly $AgBiS_2$ nanocrystals. *Nat. Photon* **2016**, *10*, 521−525.
(4) Livache, C.; Martinez, B.; Goubet, N.; Greboval, C.; Qu, J.; Chu, A.; Royer, S.; Ithurria, S.; Silly, M. G.; Dubertret, B.; Lhuillier, E. A colloidal quantum dot infrared photodetector and its use for intraband detection. *Nat. Commun.* **2019**, *10*, 1−10.
(5) Yakunin, S.; Sytnyk, M.; Kriegner, D.; Shrestha, S.; Richter, M.; Matt, G. J.; Azimi, H.; Brabec, C. J.; Stangl, J.; Kovalenko, M. V.; et al. Detection of X-ray photons by solution-processed lead halide perovskites. *Nat. Photon* **2015**, *9*, 444−449.
(6) Vafaie, M.; Fan, J. Z.; Najarian, A. M.; Ouellette, O.; Sagar, L. K.; Bertens, K.; Sun, B.; de Arquer, F. P. G.; Sargent, E. H. Colloidal quantum dot photodetectors with 10-ns response time and 80% quantum efficiency at 1550 nm. *Matter* **2021**, *4*, 1042−1053.
(7) Yang, Y.; Zheng, Y.; Cao, W.; Titov, A.; Hyvonen, J.; Manders, J. R.; Xue, J.; Holloway, P. H.; Qian, L. High-efficiency light-emitting devices based on quantum dots with tailored nanostructures. *Nat. Photon* **2015**, *9*, 259.

(8) Kim, D.; Fu, Y.; Kim, S.; Lee, W.; Lee, K.-H.; Chung, H. K.; Lee, H.-J.; Yang, H.; Chae, H. Polyethylenimine ethoxylated-mediated all-solution-processed high-performance flexible inverted quantum dot-light-emitting device. *ACS Nano* **2017**, *11*, 1982−1990.
(9) Konstantatos, G.; Sargent, E. H. Solution-processed quantum dot photodetectors. *Proc. IEEE* **2009**, *97*, 1666−1683.
(10) García de Arquer, F. P.; Armin, A.; Meredith, P.; Sargent, E. H. Solution-processed semiconductors for next-generation photodetectors. *Nat. Rev. Mater.* **2017**, *2*, 16100.
(11) Zhang, Y.; Hellebusch, D. J.; Bronstein, N. D.; Ko, C.; Ogletree, D. F.; Salmeron, M.; Alivisatos, A. P. Ultrasensitive photodetectors exploiting electrostatic trapping and percolation transport. *Nat. Commun.* **2016**, *7*, 11924.
(12) Kannan, H.; Stavro, J.; Mukherjee, A.; Léveillé, S.; Kisslinger, K.; Guan, L.; Zhao, W.; Sahu, A.; Goldan, A. H. Ultralow Dark Currents in Avalanche Amorphous Selenium Photodetectors Using Solution-Processed Quantum Dot Blocking Layer. *ACS Photonics* **2020**, *7*, 1367−1374.
(13) Kannan, H.; Stavro, J.; Mukherjee, A.; Léveillé, S.; Kisslinger, K.; Guan, L.; Zhao, W.; Sahu, A.; Goldan, A.Solution-Processed Ceria Interface Layer for Enhancing Performance of Avalanche Amorphous-Selenium Photodetectors. *2020 IEEE Nucl. Sci. Symp. and M Conf Rec (NSS/MIC)*. 2020; pp 1−3.
(14) Scheuermann, J. R.; et al. Toward scintillator high-gain avalanche rushing photoconductor active matrix flat panel imager (SHARP-AMFPI): initial fabrication and characterization. *Med. Phys.* **2018**, *45*, 794−802.
(15) Tsuji, K.; Ohshima, T.; Hirai, T.; Gotoh, N.; Tanioka, K.; Shidara, K. Ultra-High-Sensitive Image Pickup Tubes Using Avalanche Multiplication in a-Se. *MRS Online Proceedings Library (OPL)* **2011**, *219*, na.
(16) Mukherjee, A.; Vasileska, D.; Akis, J.; Goldan, A. H. Monte carlo solution of high electric field hole transport processes in avalanche amorphous selenium. *ACS omega* **2021**, *6*, 4574−4581.
(17) Mukherjee, A.; Akis, R.; Vasileska, D.; Goldan, A. A Monte Carlo solution to hole transport processes in avalanche selenium semiconductors. *Phys. and Simulation of Optoelectronic Devices* **2020**, *XXVIII*, 112740U.
(18) Mukherjee, A.; Vasileska, D.; Goldan, A. Hole transport in selenium semiconductors using density functional theory and bulk Monte Carlo. *J. Appl. Phys.* **2018**, *124*, 235102.
(19) LaBella, A.; Stavro, J.; Léveillé, S.; Zhao, W.; Goldan, A. H. Picosecond Time Resolution with Avalanche Amorphous Selenium. *ACS Photonics* **2019**, *6*, 1338−1344.
(20) Ho, L. T. T.; Mukherjee, A.; Vasileska, D.; Akis, J.; Stavro, J.; Zhao, W.; Goldan, A. H. Modeling Dark Current Conduction Mechanisms and Mitigation Techniques in Vertically Stacked Amorphous Selenium-Based Photodetectors. *ACS Appl. Electron. Mater.* **2021**, *3*, 3538−3546.
(21) Osedach, T. P.; Geyer, S. M.; Ho, J. C.; Arango, A. C.; Bawendi, M. G.; Bulović, V. Lateral heterojunction photodetector consisting of molecular organic and colloidal quantum dot thin films. *Appl. Phys. Lett.* **2009**, *94*, 043307.
(22) Kang, M. S.; Sahu, A.; Norris, D. J.; Frisbie, C. D. Size-dependent electrical transport in CdSe nanocrystal thin films. *Nano Lett.* **2010**, *10*, 3727−3732.
(23) Jung, E. H.; Chen, B.; Bertens, K.; Vafaie, M.; Teale, S.; Proppe, A.; Hou, Y.; Zhu, T.; Zheng, C.; Sargent, E. H. Bifunctional surface engineering on SnO2 reduces energy loss in perovskite solar cells. *ACS Energy Lett.* **2020**, *5*, 2796−2801.
(24) Yang, C.; Du, P.; Dai, Z.; Li, H.; Yang, X.; Chen, Q. Effects of illumination direction on the surface potential of CH3NH3PbI3 perovskite films probed by Kelvin probe force microscopy. *ACS Appl. Mater. Interfaces* **2019**, *11*, 14044−14050.
(25) Peng, M.; Ma, Y.; Zhang, L.; Cong, S.; Hong, X.; Gu, Y.; Kuang, Y.; Liu, Y.; Wen, Z.; Sun, X. All-Inorganic CsPbBr3 Perovskite Nanocrystals/2D Non-Layered Cadmium Sulfide Selenide for High-Performance Photodetectors by Energy Band Alignment Engineering. *Adv. Funct. Mater.* **2021**, *31*, 2105051.
(26) Koscher, B. A.; Swabeck, J. K.; Bronstein, N. D.; Alivisatos, A. P. Essentially trap-free CsPbBr3 colloidal nanocrystals by post-synthetic thiocyanate surface treatment. *J. Am. Chem. Soc.* **2017**, *139*, 6566−6569.
(27) Chiang, T.; Himpsel, F. J. In *Electronic Structure of Solids: Photoemission Spectra and Related Data*; Goldmann, A., Koch, E.-E., Eds.; SpringerMaterials, 1989; Vol. *23A*, pp 95−98.
(28) Brown, P. R.; Kim, D.; Lunt, R. R.; Zhao, N.; Bawendi, M. G.; Grossman, J. C.; Bulovic, V. Energy level modification in lead sulfide quantum dot thin films through ligand exchange. *ACS Nano* **2014**, *8*, 5863−5872.
(29) Boles, M. A.; Ling, D.; Hyeon, T.; Talapin, D. V. The surface science of nanocrystals. *Nat. Mater.* **2016**, *15*, 141−153.
(30) Abbaszadeh, S.; Allec, N.; Ghanbarzadeh, S.; Shafique, U.; Karim, K. S. Investigation of hole-blocking contacts for high-conversion-gain amorphous selenium detectors for x-ray imaging. *IEEE Trans. Electron Devices* **2012**, *59*, 2403−2409.
(31) Mashford, B. S.; Stevenson, M.; Popovic, Z.; Hamilton, C.; Zhou, Z.; Breen, C.; Steckel, J.; Bulovic, V.; Bawendi, M.; Coe-Sullivan, S.; et al. High-efficiency quantum-dot light-emitting devices with enhanced charge injection. *Nat. Photon* **2013**, *7*, 407−412.
(32) Pfister, G.; Lakatos, A. One-Carrier and Two-Carrier Steady-State Space-Charge-Limited Currents in Amorphous Selenium Films. *Phys. Rev. B* **1972**, *6*, 3012.
(33) Oertel, D. C.; Bawendi, M. G.; Arango, A. C.; Bulović, V. Photodetectors based on treated CdSe quantum-dot films. *Appl. Phys. Lett.* **2005**, *87*, 213505.
(34) Clifford, J. P.; Konstantatos, G.; Johnston, K. W.; Hoogland, S.; Levina, L.; Sargent, E. H. Fast, sensitive and spectrally tuneable colloidal-quantum-dot photodetectors. *Nat. Nanotechnol.* **2009**, *4*, 40.
(35) Jin, Y.; Wang, J.; Sun, B.; Blakesley, J. C.; Greenham, N. C. Solution-processed ultraviolet photodetectors based on colloidal ZnO nanoparticles. *Nano Lett.* **2008**, *8*, 1649−1653.
(36) Elward, J. M.; Chakraborty, A. Effect of dot size on exciton binding energy and electron−hole recombination probability in CdSe quantum dots. *J. Chem. Theory Comput.* **2013**, *9*, 4351−4359.
(37) Ahmadi, M.; Wu, T.; Hu, B. A review on organic−inorganic halide perovskite photodetectors: device engineering and fundamental physics. *Adv. Mater.* **2017**, *29*, 1605242.
(38) Sutherland, B. R.; Johnston, A. K.; Ip, A. H.; Xu, J.; Adinolfi, V.; Kanjanaboos, P.; Sargent, E. H. Sensitive, fast, and stable perovskite photodetectors exploiting interface engineering. *ACS Photonics* **2015**, *2*, 1117−1123.
(39) Konstantatos, G.; Howard, I.; Fischer, A.; Hoogland, S.; Clifford, J.; Klem, E.; Levina, L.; Sargent, E. H. Ultrasensitive solution-cast quantum dot photodetectors. *Nature* **2006**, *442*, 180−183.
(40) Ji, C.; Kim, K.; Oh, S. High-detectivity perovskite-based photodetector using a Zr-doped TiOx cathode interlayer. *RSC Adv.* **2018**, *8*, 8302−8309.
(41) Lee, J.-S.; Kovalenko, M. V.; Huang, J.; Chung, D. S.; Talapin, D. V. Band-like transport, high electron mobility and high photoconductivity in all-inorganic nanocrystal arrays. *Nat. Nanotechnol.* **2011**, *6*, 348−352.
(42) Hegg, M. C.; Horning, M. P.; Baehr-Jones, T.; Hochberg, M.; Lin, L. Y. Nanogap quantum dot photodetectors with high sensitivity and bandwidth. *Appl. Phys. Lett.* **2010**, *96*, 101118.
(43) Kumar, H.; Kumar, Y.; Mukherjee, B.; Rawat, G.; Kumar, C.; Pal, B. N.; Jit, S. Electrical and optical characteristics of self-powered colloidal CdSe quantum dot-based photodiode. *IEEE J. Quantum Electron.* **2017**, *53*, 1−8.
(44) Kumar, H.; Kumar, Y.; Rawat, G.; Kumar, C.; Mukherjee, B.; Pal, B. N.; Jit, S. Colloidal CdSe quantum dots and PQT-12-based low-temperature self-powered hybrid photodetector. *IEEE Photon. Technol. Lett.* **2017**, *29*, 1715−1718.
(45) Konstantatos, G.; Badioli, M.; Gaudreau, L.; Osmond, J.; Bernechea, M.; de Arquer, F. P. G.; Gatti, F.; Koppens, F. H. L. Hybrid graphene-quantum dot phototransistors with ultrahigh gain. *Nat. Nanotechnol.* **2012**, *7*, 363−8.

https://doi.org/10.1021/acsphotonics.2c01353
ACS Photonics 2023, 10, 134−146

(46) Konstantatos, G.; Clifford, J.; Levina, L.; Sargent, E. H. Sensitive solution-processed visible-wavelength photodetectors. *Nat. Photon* **2007**, *1*, 531−534.
(47) Kim, J. Y.; Adinolfi, V.; Sutherland, B. R.; Voznyy, O.; Kwon, S. J.; Kim, T. W.; Kim, J.; Ihee, H.; Kemp, K.; Adachi, M.; et al. Single-step fabrication of quantum funnels via centrifugal colloidal casting of nanoparticle films. *Nat. Commun.* **2015**, *6*, 7772.
(48) Guo, F.; Yang, B.; Yuan, Y.; Xiao, Z.; Dong, Q.; Bi, Y.; Huang, J. A nanocomposite ultraviolet photodetector based on interfacial trap-controlled charge injection. *Nat. Nanotechnol.* **2012**, *7*, 798−802.
(49) Kung, S.-C.; Xing, W.; van der Veer, W. E.; Yang, F.; Donavan, K. C.; Cheng, M.; Hemminger, J. C.; Penner, R. M. Tunable photoconduction sensitivity and bandwidth for lithographically patterned nanocrystalline cadmium selenide nanowires. *ACS Nano* **2011**, *5*, 7627−7639.
(50) Xing, W.; Kung, S.-C.; van der Veer, W. E.; Yan, W.; Ayvazian, T.; Kim, J. Y.; Penner, R. M. High-throughput fabrication of photoconductors with high detectivity, photosensitivity, and bandwidth. *ACS Nano* **2012**, *6*, 5627−5634.

https://doi.org/10.1021/acsphotonics.2c01353
ACS Photonics 2023, 10, 134−146